NMR Velocimetry of Flow in Model Fixed-Bed Reactors of Low Aspect Ratio

Xiaohong Ren

Lehrstuhl für Makromolekulare Chemie and Magnetic Resonance Center (MARC), ITMC, RWTH Aachen, 52074, Germany

and

College of Material Science and Chemical Engineering, Zhejiang University, Hangzhou, 310027, P.R. China

Siegfried Stapf and Bernhard Blümich
Lehrstuhl für Makromolekulare Chemie and Magnetic Resonance Center (MARC), ITMC, RWTH Aachen, 52074, Germany

The velocity distributions of flow of a single fluid phase through packed beds of various geometrical properties were investigated by combining magnetic resonance imaging (MRI) with velocity-encoding and pulsed-field-gradient nuclear magnetic resonance (PFG-NMR) experiments. The beds were generated from random packings of spherical glass beads and commercial porous catalyst pellets with spherical and cylindrical shape of different sizes d_p inside cylindrical tubes of diameter d_t. Flow investigations were performed for reduced dimensionless tube diameters d_t/d_p (aspect ratio) in the range 1.4–32. The influence of pellet ordering effects on the distribution of flow channels is demonstrated using static and velocity encoded spin density images. The velocity distribution averaged over the radial coordinate in the tube follows an oscillatory pattern that largely reflects the ordering of the particles themselves. This is found for spheres and, although less pronounced, for irregularly shaped catalyst particles. In all cases, flow occurs mainly along a few backbone branches, constituting a small fraction of the total cross section of the reactor. With the exception of large aspect ratios, the dominating contribution to flow occurs near the inner tube wall. The evolution of the relative fractions of flowing and stagnant fluid is discussed as a function of encoding time, and time-dependent dispersion coefficients are obtained for the preasymptotic case. © 2005 American Institute of Chemical Engineers *AIChE J,* 51: 392–405, 2005
Keywords: packed beds, magnetic resonance imaging (MRI), velocity imaging, dispersion coefficient

Introduction

A detailed knowledge of the fluid flow profile is essential for a proper design of fixed-bed reaction processes. Because of the nonuniform radial distribution of voidage, permeability, and interstitial velocity in a critical region close to the wall, the ratio of tube diameter (d_t) to particle diameter (d_p) (that is, the aspect ratio) may influence transport properties in fixed-bed catalytic reactors. One further factor determining the efficiency of this type of reactors is the property of the fluid in quasi-stagnant pools, which essentially does not take part in the flow process. Such stagnant fractions are found not only within the pore space of the catalyst pellets, but also in fluid pockets between the pellets that do not connect to the flow backbone.

The residence time of fluid elements in these pools is assumed to be mainly determined by displacements achieved as a result of self-diffusion and is an important factor influencing the reaction efficiency.

A large body of literature is available dealing predominantly with averaged, statistical quantities such as dispersion coefficients, mixing properties, or reaction efficiencies for multicomponent fluids. A more detailed investigation of the flow properties can be achieved by obtaining velocity distributions as a function of time, or by spatially resolved velocity encoding, which allows one to relate the averaged velocity of the fluid with topological features of the porous system. Nuclear magnetic resonance (NMR), with its capability of sensing positional and motional properties in a noninvasive way and combining it with chemical selectivity, has been used as a favorable means to study flow in structured media for about a decade. Apart from model samples such as random packings of spherical particles (Amin et al., 1997; Callaghan et al., 2000, 2001; Lebon et al., 1996, 1997; Maier et al., 1998; Manz et al., 1999a; Seymour et al., 1996, 1997; Shattuck et al., 1991, 1995; Tessier et al., 1997), pulsed-field gradient (PFG)–NMR has been applied to selected systems of technical importance, such as chromatographic columns (Park et al., 1999; Tallarek et al., 1998a,b,c), packed bed reactors (Gladden, 1999; Mantle et al., 2001), transport in geological media (Mansfield et al., 1996; Packer et al., 1996; Sheppard et al., 2003; Waggoner et al., 1996), two-phase flow in mixers (Rombach et al., 1998), in oil recovery (Chen et al., 1993; Tessier et al., 1998), and in reactors (Gladden et al., 2002, 2003b). Even velocity measurements of gases have become possible (Codd et al., 2003; Koptyug et al., 2000, 2001; Mair et al., 2003). Reviews of applications of flow NMR can be found in Caprihan et al. (1990) and Fukushima (1999) for general topics and in Gladden (1999, 2003a) for applications to chemical engineering problems.

For some examples, comparisons with numerical simulations were provided (Damion et al., 2000; Lebon et al., 1996; Manz et al., 1999b; Tessier et al., 1997). To achieve a good representation of the true pore space by the reconstructed geometry of the simulations, one usually avoids the presence of edge effects and assumes periodic boundary conditions, which are equivalent to an "infinite" medium. It is commonly accepted that edge effects become negligible for the statistical description as soon as the aspect ratio exceeds 30 to 40 (Ahn et al., 1986; Carbonell, 1980; Hsiang et al., 1977; Martin, 1978). For many technical applications, however, it is of great importance to understand the radial dependency of the flow properties for cases where these effects can no longer be neglected. Increased flow velocities near the inner tube wall and heterogeneous velocity distributions inside the packing affect the local reaction rate and the heat dissipation of exothermic reactions. Despite the considerable number of publications, systematic investigations for small dimensionless tube diameters d_t/d_p have not been undertaken, especially for nonspherical particles. NMR imaging techniques, combined with velocity encoding to provide local velocities averaged over times of typically 10 ms, can directly visualize the distribution of flow velocities within the porous matrix.

In this paper, we compare spatially resolved (velocity imaging) and integrated (dispersion coefficients) flow measurements by PFG-NMR in random packs of nonporous beads with dimensionless tube diameters in the range of 1.3–32, and of technical porous catalyst bed reactor particles of spherical and cylindrical shape. The purpose of this work is to demonstrate the nature of the flow distribution in packed beds of different particle sizes and shapes, and its deviation from an "ideal" case of homogeneous flow with a time-independent dispersion coefficient.

Theory of Nuclear Magnetic Resonance Imaging and Velocity Encoding

Spatial encoding in NMR imaging is based on the dependency of the resonance frequency on the strength of the magnetic field. If the magnetic field consists of a homogeneous contribution $\mathbf{B}_0 = (0, 0, B_0)$ and an additional field with a spatially constant gradient

$$\mathbf{g} = \left(\frac{\partial B_z}{\partial x}, \frac{\partial B_z}{\partial y}, \frac{\partial B_z}{\partial z} \right)$$

the Larmor precession frequency of a spin species of gyromagnetic ratio γ is given by

$$\omega(\mathbf{r}) = -\gamma[\mathbf{B}_0 + \mathbf{g}(t)\mathbf{r}(t)] \tag{1}$$

For time-invariant gradient and position vector, $\omega(\mathbf{r})$ depends linearly on the position of the spins in the direction of the applied gradient $\mathbf{g}$. The Fourier transform of the impulse response acquired in such a linear field gives a one-dimensional distribution of spin densities, or a profile of the sample, thus the name "frequency encoding." If the magnetic field gradient is applied before acquisition for a duration δ in a pulselike fashion, the spatial dependency of the Larmor frequency gives rise to a phase shift $\phi(\mathbf{r}) = \gamma\delta\mathbf{gr} = 2\pi\mathbf{kr}$, which correlates the position of spins with the phase of their resonance signal. The variable $\mathbf{k} = (2\pi)^{-1}\gamma\delta\mathbf{g}$ is called the position wave vector and has the dimension of reciprocal length. To separate the combined contributions of all spins in the sample, the wave vector is varied and the positional information is extracted after Fourier transformation with respect to $\mathbf{k}$. The so-called phase-encoding scheme thus requires a series of individual data acquisitions. Frequency and phase encoding can be combined to generate two- and three-dimensional spin density images. A standard imaging sequence, used in this study, is shown in Figure 1a.

Although a single gradient pulse labels particle *positions*, a twofold phase encoding, using a gradient pair with equal but opposite effective amplitude $\mathbf{g}$ separated by a time interval Δ, is sensitive to particle *displacements* during this interval. To symbolize the difference between the Fourier conjugate variables to position and displacement, PFG-NMR terminology defines the displacement wave vector $\mathbf{q}$ by $\mathbf{q} = (2\pi)^{-1}\gamma\delta\mathbf{g}$, which is formally identical to $\mathbf{k}$. In full equivalence to the principle of phase-encoded imaging, Fourier transformation of the signal function $E(\mathbf{q}, \Delta)$ with respect to $\mathbf{q}$ renders the distribution of displacements between initial and final position, $\mathbf{R} = \mathbf{r}_2 - \mathbf{r}_1$ (Callaghan, 1991):
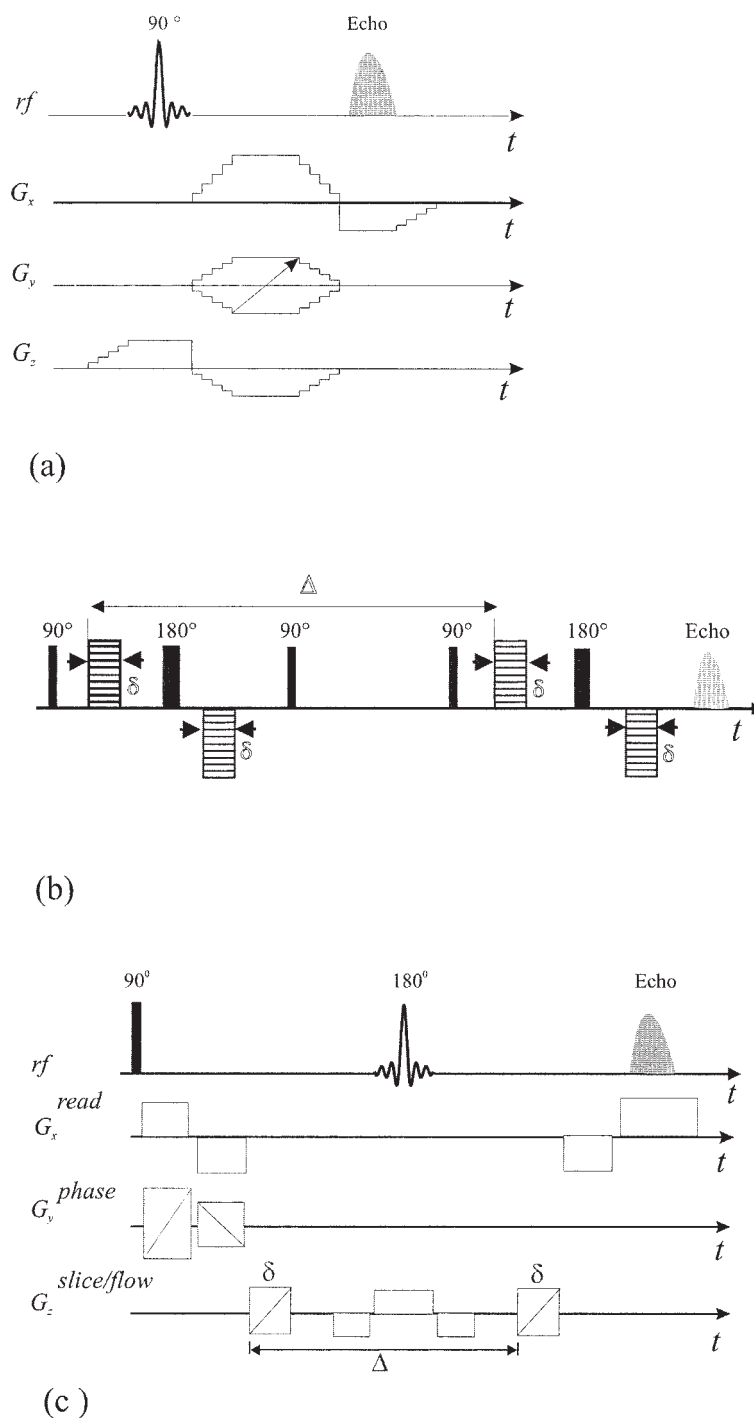
Figure 1. Pulse sequences: (a) Gradient echo single-slice imaging sequence; (b) 13-interval alternating PGSTE (APGSTE) sequence; (c) spin echo–based imaging sequence with additional velocity/propagator encoding.

$$E(\mathbf{q}, \Delta) = S(\mathbf{q}, \Delta)/S(0, \Delta)$$

$$= \int \bar{P}(\mathbf{R}, \Delta)\exp[i2\pi\mathbf{q}\mathbf{R}(\Delta)]d\mathbf{R} \qquad (2)$$

The so-called average propagator, $\bar{P}(\mathbf{R}, \Delta)$, is obtained (Kärger et al., 1983) from the distribution of starting positions $\rho(\mathbf{r}_1)$ and

the conditional probability of displacements from $\mathbf{r}_1$ to $\mathbf{r}_2 = \mathbf{r}_1 + \mathbf{R}$ during Δ:

$$\bar{P}(\mathbf{R},\Delta) = \int \rho(\mathbf{r}_1) P(\mathbf{r}_1|\mathbf{r}_1 + \mathbf{R}, \Delta)d\mathbf{r}_1 \qquad (3)$$

This relation is strictly true only if $\delta \ll \Delta$.

Figure 1b shows the pulsed-gradient stimulated echo (PG-STE) sequence used in this study. By varying the time between the second and third 90° pulse, displacements over a wide range of different encoding times Δ could be determined. Based on these propagator encodings, stagnant fluid fractions and dispersion coefficients were obtained in this study (see the Experimental section for a more detailed discussion).

The sequence of Figure 1b can, in principle, be combined with a two- or three-dimensional imaging sequence to measure the full propagator for each volume element (see Figure 1c). However, it is often sufficient to determine the average velocity, in which case the imaging module is supplemented by a pair of gradient pulses of fixed amplitude. If the experiment is performed with and without the velocity encoding step, the phase shift obtained from the difference of the phase value at each pixel in both images is proportional to the local displacement during Δ, $\phi = 2\pi q v \Delta = \gamma \delta g v \Delta$ and one can thus attribute the local *averaged* velocity to each pixel as an additional imaging information.

Dispersion in Porous Media

For a certain range of technical and engineering requirements, it is customary to describe the dispersion coefficients of fluid flow through pipes or a porous medium as the diagonal elements of the long-time, asymptotic limit of the dispersion tensor. The dispersion tensor describes the spread $\mathbf{u}(t)$ of individual *particle* (or, more generally, *fluid element*) velocities, $\mathbf{v}(t)$, relative to the average velocity, $\mathbf{V}$: $\mathbf{u}(t) = \mathbf{v}(t) - \mathbf{V}$. Here, $\mathbf{v}(t)$ denotes the time-dependent, local velocity and the average $\mathbf{V}$ is given by $\mathbf{V} = \lim_{t\to\infty} \langle \mathbf{v}(t) \rangle$, where the ensemble average $\langle \cdots \rangle$ is taken over the distribution of velocity fields localized in space (Koch et al., 1987a,b). The long-time limit is taken with respect to the longest correlation times of the velocity fluctuations (Brady, 1990). The asymptotic dispersion tensor is then described by

$$\mathbf{D*} = \lim_{t\to\infty} \int_0^t sym\langle \mathbf{u}(\tau) \otimes \mathbf{u}(0) \rangle d\tau \qquad (4)$$

where $sym(A) = 1/2(A + A')$ and $\langle \mathbf{u}(\tau) \otimes \mathbf{u}(0) \rangle$ is the velocity autocorrelation function. Because of the natural boundary conditions of the fixed-bed array, the net flow in transverse direction vanishes, and the average of the longitudinal or z component of $\langle \mathbf{v} \rangle$, also called the Dupuit–Forcheimer velocity (Bear, 1975), remains constant for all times.

Although it is possible to experimentally determine all components of the dispersion tensor, we will be concerned with only its diagonal elements. In the asymptotic limit, this trace of the dispersion tensor is related to the mean-squared displacements by

$$\mathrm{Tr}(D*) = \lim_{t\to\infty} \frac{1}{2} \frac{d\sigma^2}{dt} \qquad (5)$$

where $\sigma^2 = \langle [\mathbf{r}(t) - \langle \mathbf{r}(t) \rangle]^2 \rangle$.

In many cases, the conditions leading to an asymptotic behavior of the dispersion process are not fulfilled. Even for industrial-size fixed beds, it is important to understand the preasymptotic region of dispersion. The NMR experiments mainly focus on this region because the sensitive volume is restricted by the geometry of the receiver coils. In the preasymptotic regime, the heterogeneity of the matrix—and thus of the velocity field—has to be taken into account and a nonlocal model of the dispersion process becomes necessary. The nonlocal dispersion tensor now depends on time and space and is given by (Koch et al., 1987a,b):

$$D*(\mathbf{r} - \mathbf{r}', t - t') = \langle \mathbf{u}(\mathbf{r}, t) P(\mathbf{r}, t | \mathbf{r}', t') \mathbf{u}(r', t') \rangle \qquad (6)$$

where $P(\mathbf{r}, t | \mathbf{r}', t')$ is the transition probability that a fluid element moves from $\mathbf{r}$ at t to $\mathbf{r}'$ at t'.

Although the cross-over toward the asymptotic regime is determined by a variety of factors and clearly depends on the flow rate, it is generally true that the dispersion tensor elements become time-independent only for displacements that substantially exceed the structural size of the porous medium; there is a discussion in the literature whether an asymptotic limit can actually be reached at all (Koch et al., 1998; Lowe et al., 1996). A convenient definition is given by the time it takes a fluid element moving at $\langle v \rangle$ to cross this characteristic length scale d of the system

$$\tau_c = \frac{d}{\langle v \rangle} \qquad (7)$$

For the samples discussed in this study, d is related to the particle size but its precise definition is not necessarily straightforward for the cylindrical catalyst pellets. Moreover, several recent studies have shown that larger-scale heterogeneities have a distinct influence on the dispersion behavior (Khrapitchev et al., 2002, 2003; Maier et al., 1999, 2002). These can be packing heterogeneities that lead to spatially varying porosities even when averaged over volumes containing many beads or particles. The longest relevant timescale is given by the extension of the representative elementary volume (REV) (Bear, 1975; Plumb et al., 1990; Whitaker, 1986). The REV is the smallest volume containing all morphological features that exist in the porous medium with their global statistical weighting. It is therefore often more reasonable to speak of a distribution of correlation times, $P(\tau_c)$, but we will retain the concept of an average τ_c to facilitate a better comparison of the results in dimensionless units of displacements.

In this context, it is appropriate to define two further quantities that are frequently used to describe properties of flow. The Péclet number is essentially the ratio of the time taken to diffuse across a pore of characteristic size l, and the time to flow across it:

$$\mathrm{Pe} = \frac{l\langle v \rangle}{D_0} \qquad (8)$$

where D_0 is the molecular self-diffusion coefficient. In the case of bead packs it is usual practice (Koplik et al., 1988; Quintard et al., 1993) to take the characteristic dimension l as being given by the effective pore diameter, defined by

Table 1. Physical Properties of the Packed Porous Particles*

Material	Molecular sieve 5 Å	Pt/Ni catalyst: G-43	Pt/Re catalyst: E-802
Manufacturer	Carl Roth, Germany	Südchemie, Germany	Engelhard, USA
Shape	Spherical (Type A)	Cylindrical (Type B)	Cylindrical (Type C)
Pellet size	⌀2 mm	⌀4.5 × 4.5 mm	⌀1.5–2 × 3–8 mm
Equivalent diameter	⌀2 mm	⌀4.5 mm	⌀2.2 mm (average)
T_1 (ms)	16.6	9.8	290
T_2 (ms)	11.3	4.4	13.0

*The relaxation times were determined at a Larmor frequency of 300 MHz for protons of water adsorbed into saturated catalyst pellets (average error 2%). See text for more details.

$$l = \frac{\varepsilon d_p}{1 - \varepsilon} \qquad (9)$$

By taking into account average particle dimensions, we will assume this definition of the Péclet number throughout this paper. The second dimensionless hydrodynamic quantity is the well-known Reynolds number (Re), which indicates the ratio of inertial and viscous forces and is defined by

$$\mathrm{Re} = \frac{l\langle v \rangle}{\nu} \qquad (10)$$

where ν is the kinematic viscosity of the liquid. It is sufficient to state that within the range of water flow velocities and particle sizes used in this study, Re is found to be in the range 10–400, which ensures laminar conditions throughout all the experiments.

For a catalyst bed design, not only are the dispersion coefficient averaged over the whole sample and its time dependency of interest, one would rather like to investigate the distribution of streamlines in the porous matrix. For instance, it would be desirable to produce an even distribution of streamlines that provides contact of the streaming fluid with all catalyst pellets at similar probability and contact time. It is therefore important to obtain information about the local distribution of velocities on timescales well below the onset of mechanical dispersion, that is, for times much shorter than τ_c. The determination of local velocities as well as averaged propagators and dispersion coefficients will thus be combined in this work.

Experimental

The samples consisted of a glass tube (19 mm inner diameter; 300 mm length) that initially had been filled with bidistilled water. They were prepared by adding a mixture of water and particles (glass beads and catalyst pellets, respectively) to the water-filled container and the packing was regularly stirred to avoid trapping of air bubbles. The samples containing porous catalyst pellets were saturated with water before the filling process. The packings were confined between glass frits, acting as a diffuser, to provide an even distribution of streamlines at the inlet and to avoid holdup of particles at the outflow. After fixing the frits, the glass container was connected to a precision pump (BVP-Z, Ismatec) by silicone rubber tubes of approximately 2 m length, providing a constant volume flow rate of water through the packings. The flow rate was measured volumetrically and the interstitial average velocities were computed

based on the porosity of the packing that, in turn, was obtained from weight measurements.

Five types of glass beads were purchased from Carl Roth (Karlsruhe, Germany); their sizes and respective tolerances are $d_p = 13.8 \pm 0.20$, 7 ± 0.15, 4 ± 0.10, 2 ± 0.20, and 0.6 ± 0.03 mm. Three types of catalyst pellets were obtained (Carl Roth; Südchemie AG, Munich, Germany; and Engelhard Co. Iselin, NJ). Their properties are summarized in Table 1. The equivalent diameters d'_p for cylindrical pellets are calculated from the ratio of particle volume to external surface area [$d'_p = 6(V_p/A_p)$]. In the case of catalysts of Type C, we have measured an approximately Gaussian length distribution with a mean of 5.2 mm and 90% of all pellets being within 2.5 and 8.5 mm length. For the porous particles, the NMR relaxation parameters were obtained with standard pulse sequences for water-filled catalyst pellets before the imaging experiments: T_1 with inversion-recovery and T_2 with CPMG using a pulse separation of 1.5 ms.

The NMR experiments were performed on a DMX 300-MHz Bruker spectrometer equipped with a horizontal super wide bore 7 T magnet. A commercial microimaging gradient system was used, providing a maximum gradient strength of 1.2 T/m. Pure spin density images were acquired on cross sections with a thickness of 1 mm, using the sequence shown in Figure 1a, with typical echo times of 6.3 ms. The gradients were ramped in such a way as to allow the fastest possible experimental time. The resolution of the acquired images was 98×195 μm.

The sequence used for velocity-encoded imaging is shown in Figure 1c. The flow compensation gradients in the spatial dimensions were used for suppressing artifacts arising from the spin migration. Because of the short effective relaxation times influenced by magnetic field distribution inside the sample, the shortest possible gradient pulse separation was chosen so that $\Delta = 6.9$ ms, whereas the total sequence took 12 ms between encoding and acquisition. The bipolar gradients G_z were stepped in 32 steps.

To minimize the influence of transverse relaxation in the presence of the background field gradients generated by the glass/liquid interface, propagators were obtained using the alternating gradient variant (Cotts et al., 1989) of the PGSTE sequence (APGSTE; see Figure 1b) in conjunction with an appropriate phase cycle to recover the full phase information of the signal (Lucas et al., 1993). In this sequence, the cross-terms arising from the combined effect of pulsed-field gradients and background gradients are eliminated to first order by splitting each PFG into two halves, symmetrically placed about a 180° rf pulse. Displacements parallel to the main flow axis (z-direction) were measured with encoding times Δ in the range
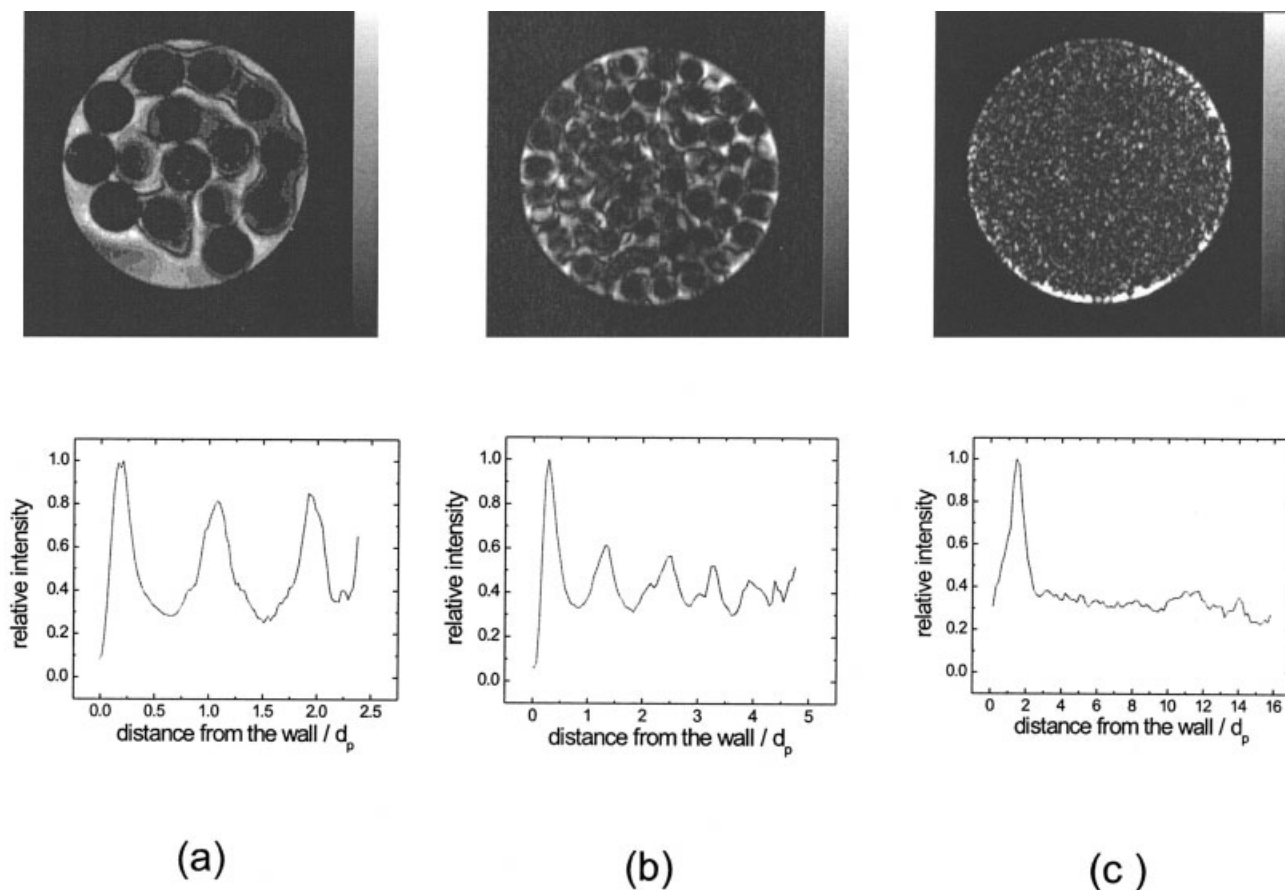
Figure 2. Spin density images (top) and radial spin density distributions (bottom) of packings of glass beads of diameters.

(a) 4 mm, (b) 2 mm, (c) 0.6 mm. The resolution of the images is 98×195 μm.

30–1200 ms; the time between the first and second 90° pulses was 5.5 ms.

Results and Discussion

Spin density imaging

Images for arrays of glass beads with 4, 2, and 0.6 mm diameter are shown in Figure 2 (top). For these bead sizes, one can assume that the slice of 1 mm thickness constitutes a sufficiently representative volume to attempt a radial density analysis. In Figure 2 (bottom), the radial density distribution of spins, normalized to the maximum porosity, is plotted for all samples. For the larger beads with low aspect ratios ($d_t/d_p =$ 4.75, 9.5), multiplayer (ringlike) arrangements attributed to the confining effect of the wall can be seen clearly. The highest spin density is observed near the tube wall and the subsequent layers, whose separation is close to d_p, are increasingly less ordered. This observation is in agreement with the data presented in Götz et al. (2002), which compares PFG-NMR with Laser Doppler Anemometry results. Similar findings were reported for different bead sizes, materials, and packing methods (for example, see Park et al., 2002; Sederman et al., 2001). For the smallest glass beads of 0.6 mm diameter ($d_t/d_p =$ 32), susceptibility effects were too strong to allow a satisfactory image representation. An increased signal intensity at the edge

of the tube is again observed, but in this case might partially be attributable to packing imperfections in the horizontal cell.

Images for random packings of catalyst particles are shown in Figure 3. Spherical catalyst pellets of 2 mm diameter (Type A, Figure 3a) show an ordering effect similar to that of glass beads and can be directly compared to the results of Figure 2b. The larger cylindrical pellets of about 4.5 mm diameter and 4.5 mm length (Type B) are expected to be packed in random orientations. The spin density image seems to support this notion, given that both circular and rectangular shapes are visible (Figure 3b). Still, ordering of the particles along the tube wall is found as is shown in the density plot of Figure 3b (bottom). The increased signal intensity near the wall is observed as well as a diffuse secondary maximum inside the first layer of particles. A considerable statistical ordering effect is even observed for the long, cylindrical pellets of catalyst Type C (see Figure 3c). At closer look, one can detect a nonzero signal inside the pellets themselves, which stems from the intraparticle water. The transverse relaxation times (T_2), however, are different, as is summarized in Table 1. Because of the exponential decay with a time constant T_2 during the pulse sequence of duration 7.8 ms, a signal loss to about 1/2 for types A and C, and to about 1/6 for type B is expected. Indeed, no intensity is found inside the pellets of type B, whereas a
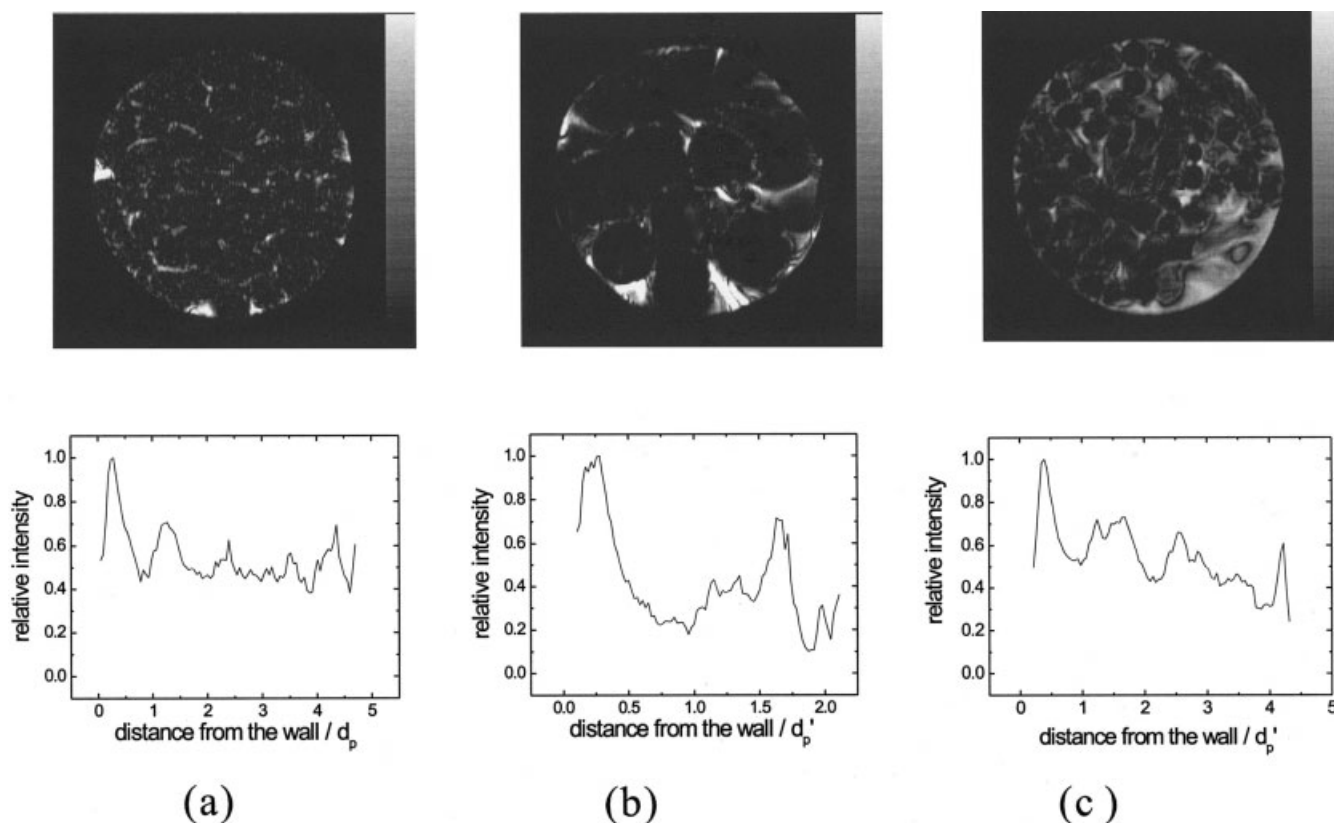
Figure 3. Spin density images (top) and radial spin density distributions (bottom) of packings of porous media.

(a) Type A, spherical molecular sieve. (b) Type B, regular cylindrical catalyst. (c) Type C, irregular cylindrical catalyst. The resolution of the images is 98×195 μm.

remaining signal is seen in types A and C. In the radially averaged plot (Figure 3 bottom), the intraporous water leads to less pronounced minima between the spin density maxima.

As a feature common to all randomly packed beds with low aspect ratio we can state the occurrence of a strong peak in the fluid distribution near the wall, which could lead to the assumption that flow is predominantly channeled through this region that possesses the smallest resistance. Ringlike arrangements of the spherical pellets can be followed up to five bead diameters, with less pronounced peaks being observed for irregularly shaped particles. From these spin density distributions alone, it is yet unclear whether flow is mostly directed along the widest channels, which would lead to an equivalent distribution of fluid velocities in the presence of a pressure gradient, or whether large voids correspond to regions of low velocity. This flow behavior is discussed in the following section.

Velocity-encoded imaging

By using the pulse sequence shown in Figure 1c, the velocity during the separation time Δ is encoded by an additional phase shift of the signal of $\phi = \gamma \delta G_z v \Delta = 2\pi \mathbf{q} v \Delta$, where $\mathbf{q}$ is the displacement wave vector. In any given pixel, the ratio of the corresponding velocity-encoded and reference image amplitudes will be

$$\frac{S_I}{S_R} = \frac{a_I}{a_R} (\cos \phi + i \sin \phi)$$

Therefore, the value of ϕ is obtained from the arc tangent of the ratio of the imaginary and real parts of the signal. To prevent phase aliasing, the velocity-encoding gradients were chosen to keep the phase shift associated with the flow in the range from $-\pi$ to π. In principle, a single gradient pair encoding step, giving rise to an additional phase shift for each pixel that is proportional to the velocity, can be sufficient if the obtained image is directly compared with the pure spin density representation. Under realistic conditions, particularly in the presence of solid/liquid interfaces, phase errors occur so that two or more encoding steps must be combined for a correction of the spurious influences. For the investigations in this study, the bipolar gradient was varied in typically 32 equidistant steps, and the average velocity was computed from those 32 q values that correspond to signal intensities above a given signal/noise threshold using linear regression algorithms.

It is important to estimate the displacement during the encoding time relative to the slice thickness or the structural sizes of the system itself. For $\Delta = 6.9$ ms and a total sequence duration of 12 ms, and considering the typical average interstitial velocities of about 20 mm/s, this corresponds to displacements of about 150 and 300 μm, respectively. This distance is generally smaller than the thickness of the excited slice. Its ratio to the particle size is given by the characteristic time τ_c, which exceeds the sequence time in all cases (see figure captions).

Velocity distributions for flow in glass bead packs with different aspect ratios are shown in Figures 4 and 5 for similar
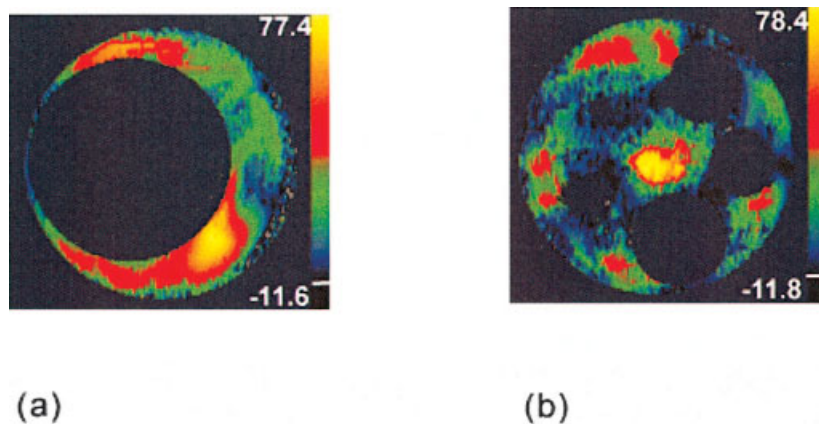
Figure 4. Velocity-encoded images for water flow at a rate of $Q = 2.93$ cm^3/s in large bead packs.

(a) $d_p = 14$ mm, $d_t/d_p = 1.4$ ($\tau_c = 800$ ms), (b) $d_p = 7$ mm, $d_t/d_p = 2.75$ ($\tau_c = 350$ ms). The resolution of the images is 195×390 μm. The unit of the velocity indicated is mm/s. The white line denotes 0.
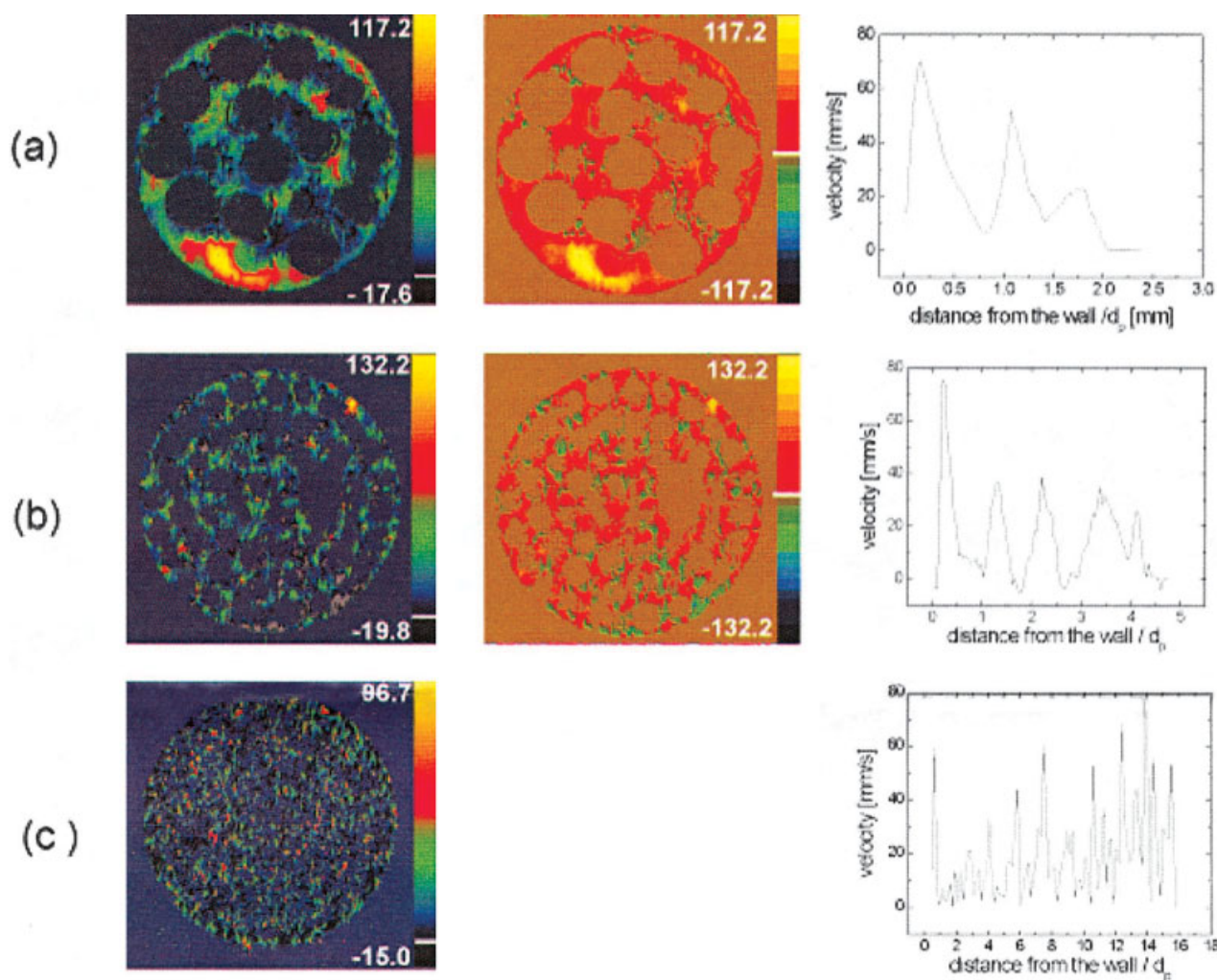

Figure 5. Velocity-encoded images (left, center) and radial velocity distributions (right) for water flow in the bead packs of Figure 2.

The center column serves for highlighting negative velocity components (green color). (a) 4-mm glass beads, $Q = 2.93$ cm^3/s ($\tau_c = 155$ ms). (b) 2-mm glass beads, $Q = 2.93$ cm^3/s ($\tau_c = 75$ ms). (c) 0.6-mm glass beads, $Q = 2.25$ cm^3/s ($\tau_c = 30$ ms). The resolution of the images is 195×390 μm.

Sample	$\langle v \rangle$ (Volumetric, mm/s)	$\langle v \rangle$ (NMR, mm/s)
Glass, 14 mm	17.2 ± 0.6	17.9 ± 1.5
Glass, 7 mm	19.5 ± 0.7	17.3 ± 1.5
Glass, 4 mm	25.8 ± 1.3	22.5 ± 2.0
Glass, 2 mm	27.1 ± 1.3	22.9 ± 2.0
Glass, 0.6 mm	19.8 ± 1.0	14.3 ± 1.5

*Flow rates are given in the respective figures.

flow rates. For the aspect ratios of 1.4, 4.75, and 9.5, the highest fluid velocities are found immediately inside the tube edge, and pronounced maxima of velocity, corresponding to the ringlike distribution of fluid between the beads, are separated by regions of slow flow, clearly a consequence of the stacking of glass spheres at different radial positions. This result is in good agreement with that of Götz et al. (2002) and Feinauer et al. (1997). It is almost identical to the velocity maxima found from modeling in Papageorgiou et al. (1995) and by anemometry in Bey et al. (1997) for a similar aspect ratio of $d_t/d_p = 5$. With increasing aspect ratio the velocity distribution becomes more even, and the channeling effect near the wall becomes smaller. For the specific aspect ratio of 2.7, however, a semiregular pentagonal arrangement is favored (a value of $d_t/d_p = 2.7013$ would allow a perfectly regular structure). Therefore, a central channel is left free through which water flows mostly unaffected by obstacles, which explains the maximum flow velocity in this region. For the smallest beads with the aspect ratio of 32, on the other hand, the velocity distribution is relatively smooth, with regions of high velocity of the order of one bead size (2–3 pixels) being discernible; preaveraging within one voxel must play a role here. The plot of $v(r)$ in Figure 5c no longer reveals a clearly identifiable periodicity, although high velocities seem to appear throughout the reactor, and a similar dominance of wall flow as for smaller aspect ratios is not observed.

Another feature that can be found here is the occurrence of backflow, which also becomes more prominent with increasing aspect ratio. In the center plot of Figure 5, negative- velocity components were highlighted by a different color scheme and can be identified in green; they are localized mostly in areas between two beads. In particular, for the aspect ratio of 9.5, larger regions of backflow become visible. Negative velocities exceeding the average flow velocity in magnitude are found, and even the radially averaged profile becomes negative at the distances with the highest solid fraction. The occurrence of negative values of velocities cannot be explained by a particular artifact such as the vicinity of the interface. The presence of backflow has been discussed in the literature (Blümich, 2000; Kutsovsky et al., 1996; Seager et al., 1991) and models have been developed that explain it by circulating flow patterns in the immediate vicinity of surfaces, but the existence of vortexlike structures at the meeting points of stream lines is an alternative explanation.

We now compare the average velocities determined from weighting the velocity in each pixel with the spin density with that from the volumetrical values in Table 2. Because of the background gradients as a consequence of the increasing influence of susceptibility differences between glass and water, the quality of the data is apparently reduced for smaller beads.

However, a deviation of 2–15% still agrees within error limits for all samples except the smallest beads. It should be noted that velocity distributions obtained for different slice positions in a system of similar aspect ratio show a comparable scatter (Park et al., 2002). Only for the beads of 0.6 mm in diameter, the combination of outflow, preaveraging (as discussed by Seymour et al., 1997), and susceptibility gradients, adding random contributions to the spin phases on scales below the imaging resolution, sum up to an average velocity that is systematically too low by about 27%. Nevertheless, the common results drawn above are still acceptable.

Figure 6 shows the velocity distribution of fluid in the randomly packed beds of the three catalyst pellets with aspect ratio, $d_t/d_{p'} = 9.5$, 4.2, and 8.6, respectively. Negative velocities are again highlighted in the center column. One notices a somewhat higher fluctuation of velocities between individual voxels compared to the glass bead packs, which is partly explained by the stronger background magnetic field gradients arising from the metal-containing catalyst pellets. These directly influence the relaxation times of the intraporous fluids (see Table 1), but also affect the field distribution in their immediate vicinity, resulting in a lower signal-to-noise ratio of the data. Because of the comparatively long duration of the pulse sequence (12 ms), almost all signal intensity from inside the pellets is lost and the remaining signal does not allow a computation of the velocity. We note that the "zero" values of velocities inside the pellets do not represent the result of a fitting procedure, but these were set to zero intentionally because they fell below a minimum signal threshold.

Results found for the irregularly shaped particles contain features in common with those of the better-known systems of bead packs. High velocities are regularly found for intermediate and narrow pores, whereas open voids are characterized by rather slow flow. Fluid transport is not evenly distributed and high velocities occur localized in regions comparable to the pellet size. Backflow is present in all investigated systems. Similar observations were made by Gladden (1999) and Klemm et al. (1997), who could attribute a flow backbone as being essentially relevant for fluid transport within the porous system, with the remaining pore space containing slow-moving fluid fractions. The radial distribution of velocities for the three catalyst systems (see Figure 6, right) shows a less regular structure, in agreement with the less strongly pronounced periodicity in local porosity. Still, the highest radially averaged velocities always occur near the tube wall. Furthermore, the breakup of the streamlines into a few individual backbone branches becomes more evident for larger values of d_t/d_p. However, the wall-slip effect has less influence on the total fluid transport, that is, the distance between the pellet surface and regions of high flux is smaller, allowing easier transport of the reactants to/from the reaction sites inside the pellets. This must be contrasted to the widely accepted simplification of an effective plug-flow behavior, which is often used to model the flow properties in reactors without taking spatial variations into account. For the design of reactors in technical applications, this can lead to an optimized aspect ratio for which the distribution of backbone branches is relatively even across the cross section of the tube, whereas a certain number of pellets is left mostly inactive. Assuming that the distribution of these branches is purely random but does not change when a given flow situation is established (otherwise, distinct maxima in the
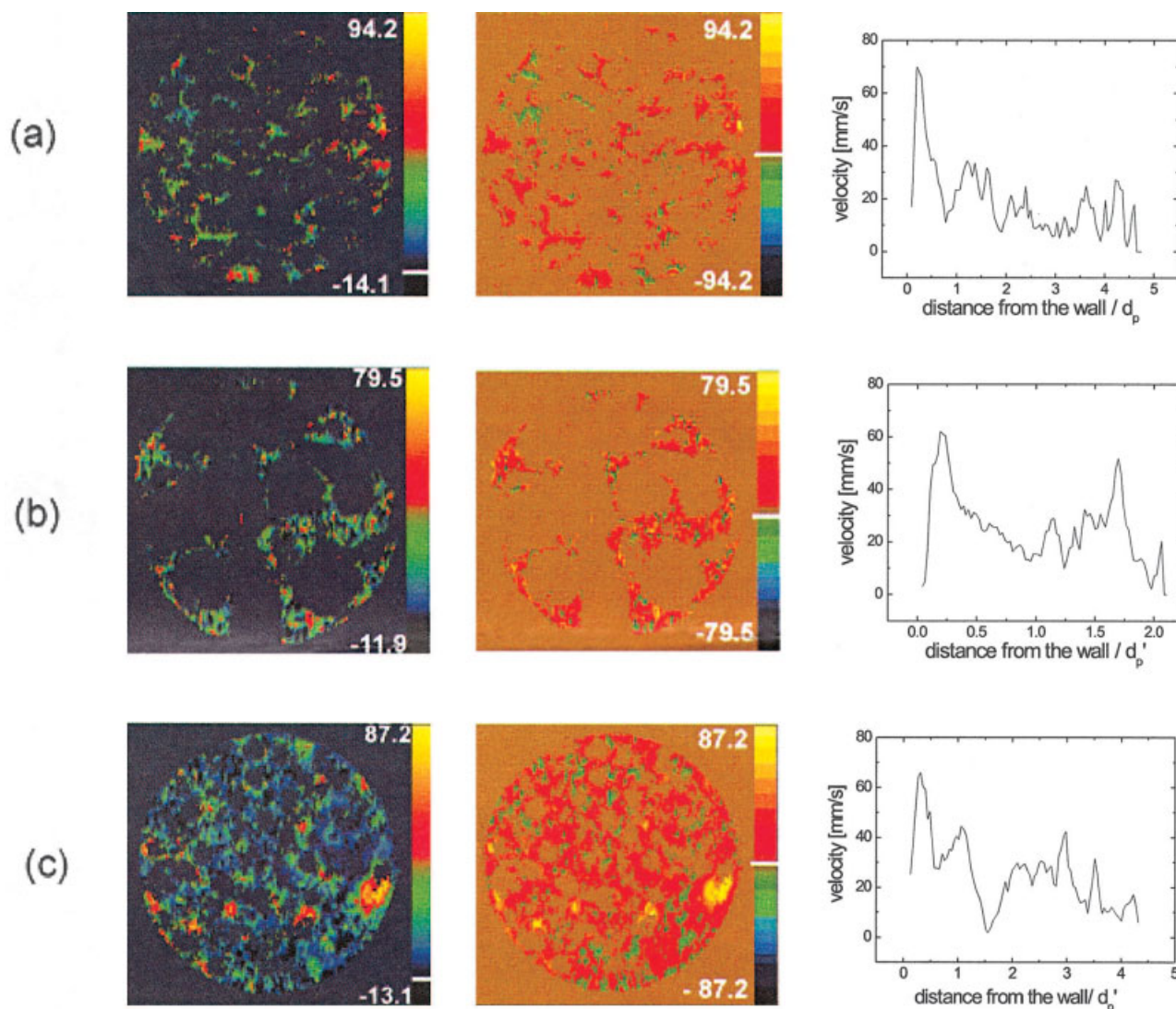
Figure 6. Velocity-encoded images (left, center) and radial velocity distributions (right) for water flow in the catalyst particle packings of Figure 3.

The center column serves for highlighting negative velocity components (green color). (a) Type A, (b) Type B, (c) Type C. The flow rate Q = 2.93 cm³/s. The resolution of the images is 195 × 390 μm.

velocity distribution would be smoothed out), loosening and repacking fixed-bed reactors with the same pellets can thus be a means of exposing the "fresh" catalyst pellets and making them available for reactions during further reaction cycles without the need to regenerate the whole bed.

The presented data are snapshots at particular volume flow rates. It is not at all clear whether the observed patterns remain valid when the flow rate is changed, or whether the flow backbone changes its shape. Literature about this topic is somewhat ambiguous; although Mansfield et al. claimed that velocity maps depend on the history before measurements at a particular flow rate, and that different flow rates favor different distributions of flow backbones (Mansfield et al., 1996, 2001), the comparison of simulated and experimental flow fields presented by Kimmich et al. clearly support a deterministic approach (Klemm et al., 2001). Because most flow experiments, including those presented in this study, were performed in horizontal setups, the influence of gravity might be a factor that
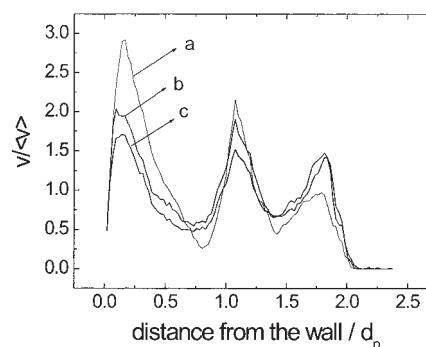

Figure 7. Radial velocity distributions for water flow in 4-mm glass beads at three different flow rates.

Here the velocity is normalized by the average velocity $\langle v \rangle$. (a) Q = 2.93 cm³/s, Re = 75, Pe = 37,000, $\langle v \rangle$ = 26 mm/s (τ_c = 155 ms). (b) Q = 6.37 cm³/s, Re = 160, Pe = 80,000, $\langle v \rangle$ = 56 mm/s (τ_c = 71 ms). (c) Q = 9.73 cm³/s, Re = 250, Pe = 125,000, $\langle v \rangle$ = 86 mm/s (τ_c = 47 ms).

should be taken into account. However, there is usually agreement about the fact that for a given setup, flow conditions are stationary so that averaging procedures will not affect interpretation of the results.

To demonstrate the influence of total flow rate on the shape of the flow backbone, the velocity distributions at three different flow rates for one example of random packings (4-mm-diameter glass beads) are compared in Figure 7. With increasing flow rate, corresponding to Reynolds numbers of Re = 75, 160, and 250, and Péclet numbers of Pe = 37,000, 80,000, and 125,000, respectively, a smoother velocity distribution in the cross section was found. Note that τ_c is still long compared to the velocity encoding time, which was kept unchanged at 6.9 ms. The radial distribution of velocities shows an evolution of the relative contributions of the three distinct rings of local maxima: slow flow is dominated by the outer ring, whereas the averaged velocities in each ring become almost identical for the highest flow rate. For the particular system under study, we find that the distribution of flow lines becomes more even at higher flow rates, but it cannot be concluded whether this is true for any combination of d_t/d_p and both Péclet and Reynolds numbers. Varying the flow rate, however, can be assumed to affect the velocity field in the fixed bed in general, and provides a further parameter for manipulating the conversion factor of the reactor by optimizing the flow distribution and the residence time of the fluid within the reactor.

Statistics of velocity distributions

The properties of fluid flow can be expressed in statistical terms by the so-called propagator. The propagator represents the displacement probability function for an ensemble of spins, usually within the entire sample or a statistically representative volume of the same. Compared to the method of velocity encoded imaging, it features three main differences: (1) the information is collected from all available spins, thus removing the spatial information but being more robust to stochastic and systematic errors arising from the much improved signal-to-noise ratio; (2) not an individual velocity averaged over a (usually) short time interval, but the total distribution of velocities in the sample is obtained, the evolution of which can be followed by varying the encoding time; and (3) the propagator is obtained by Fourier transformation along the velocity-encoding (q) dimension, which might experimentally restrict its determination to the capabilities of the spectrometer because higher gradient strengths are required compared to encoding average velocities. Furthermore, another limitation different to the one described for velocity imaging has to be considered. If no slice selection is performed, displacements of all spins inside the resonator volume are determined, but the much longer encoding times Δ have the consequence that a finite fraction of fluid elements, proportional to the displacement $v\Delta$, leaves the resonator and thus do not contribute to the signal at the point of data acquisition. Naturally, this affects the fastest spins so that large velocities are underrepresented in the final propagator if encoding times are chosen too long.

The evolution of the propagator with increasing time has been discussed in detail in the literature (Lebon et al., 1996; Packer et al., 1996; Seymour et al., 1997; Tallarek et al., 1998a; Tessier et al., 1997). For samples with large aspect ratio d_t/d_p, experimental results have been obtained and successfully com-
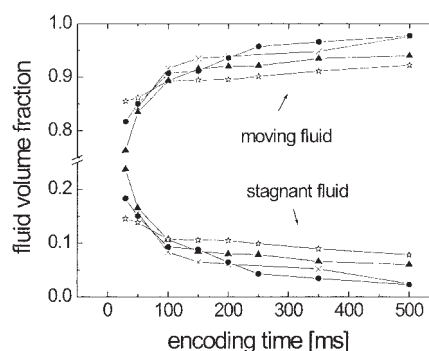

Figure 8. Dependency of stagnant and moving fluid fractions on the observation time Δ for glass beads 0.6 mm (×), 2 mm (▲), 4 mm (☆), and cylindrical catalyst Type C (○).

Q = 2.93 cm³/s (for d_p = 0.6 mm, Q = 2.25 cm³/s); fitting errors were less than ±1%.

pared to numerical simulations. Our results for the smallest glass beads (d_t/d_p = 32) are in agreement with these studies, although qualitative differences occur for larger beads. From the point of view of reactor design, however, the separation into "moving" and "stagnant" fluid fractions is more important than the exact knowledge of the velocity distribution. Stagnant fluid will not take part in reactant transport inside a working reactor, thus reducing its efficiency. The term "stagnant" relates to fluid elements in dead-end pores and near walls. They will be transported to the nearest flow backbone by a combination of diffusion and convection. There is strong evidence that fluid elements with small displacements along the main flow direction also remain "slow" in the other directions (Stapf, 2002; Stapf et al., 1998, 2000), so that the concept of stagnant pools is justified. Water inside the pores of catalyst pellets, which would contribute with a very narrow displacement distribution given by restricted diffusion, is rendered invisible by its intrinsically short relaxation time. Relaxation times of interparticle water, on the other hand, are much longer than those of the intraporous water, so that the interparticle contribution is not significantly affected. This is supported by the results of numerical simulations that showed no significant influence of the T_1 relaxation behavior, even for particles with much larger specific area (Maier et al., 2000; Tessier et al., 1997), whereas an effect on the transverse relaxation time T_2 can be expected for experimental times substantially exceeding those in this study (Britton et al., 2001). At least for the conditions and samples discussed in this study, it is therefore possible to obtain a quantitative description of intraporous stagnant fluid.

Figure 8 compares the evolution of the stagnant and flowing water fractions as a function of encoding time Δ for glass beads of 0.6, 2, and 4 mm diameter and for the Type C catalyst (cylindrical pellets). The stagnant phase is found to decrease most rapidly for the beads of smallest size. The corresponding fraction for the pellets of cylindrical shape decays similarly fast but also starts at a lower level at the shortest encoding time of Δ = 30 ms. From this result one can conclude that the rodlike shape of the pellets reduces the amount of nonflowing water compared to spherical particles of similar size, which should result in a somewhat higher reactor efficiency, given that fewer reaction sites are found in regions of immobile fluid pools. On

the experimentally accessible timescale, a small percentage of the fluid remains stagnant; this is equivalent to the notion of the preasymptotic dispersion regime where the dispersion coefficient has not yet become time independent.

To investigate the time dependency of the dispersion process, we have determined the dispersion coefficient $D^*(\Delta)$, which is given by the second moment of the propagator (the mean squared displacement). Rather than computing $D^*(\Delta)$ from the shape of the propagator directly, it is also possible to obtain it from the initial slope of the signal function $E(q, \Delta)$ in a 1D NMR experiment (Seymour et al., 1997):

$$D^*(\Delta) \approx -(4\pi^2\Delta)^{-1}\lim_{q \to 0} \frac{\partial \ln|E(q, \Delta)|}{\partial q^2}$$

This low-q behavior has the advantage that the second moment of displacements can be measured without the need of large pulsed field gradients because the signal is not required to be forced to zero to perform a correct Fourier transformation. The time-dependent dispersion coefficients are compared for 2-mm glass beads and the Type C catalyst at different flow rates, respectively, in Figures 9a and c. Moreover, the Péclet number is also changed for constant flow rate but varying bead size; the results are shown for the glass beads of different diameters (Figure 9b).

Because of the outflow effect that would reduce the measured dispersion coefficient below its real value, measurements at longer Δ could not be performed. In all our studies, the asymptotic limit is never reached, with the possible exception of the smallest particles where the value is in agreement with the dispersion coefficients obtained from the classical tracer experiments, indicating also that the wall effect is not dominant here. Still, a relative comparison of the dependency of D^* is possible. For instance, the dependency of the asymptotic (long-time) dispersion coefficient on the Péclet number known from literature is also visible in the preasymptotic range. Figure 9 suggests that all measurements were indeed taken out in the preasymptotic regime. In the case of the catalyst, however, a comparison with classical tracer methods is not possible because the latter cannot be applied in a straightforward manner, given that the tracer is absorbed into the porous pellets and saturation conditions must be achieved. NMR techniques, given that encoding times are long compared to the intraporous relaxation times, possess the advantage that the dispersion results are not affected by the porosity of the pellets. Because of these short relaxation times, signal contributions from water exchanging in and out of the pellets are suppressed. The true residence time distribution of fluid in the packed bed of porous particles thus deviates from the experimentally determined propagators because the latter measures only the extraporous fraction.

Conclusions

The velocity distributions of flow of a fluid phase through packed beds of various geometrical properties were investigated by combining magnetic resonance imaging (MRI) with velocity encoding and pulsed-field gradient nuclear magnetic resonance (PFG-NMR) experiments. The beds were generated from loose packings of glass beads and commercial porous
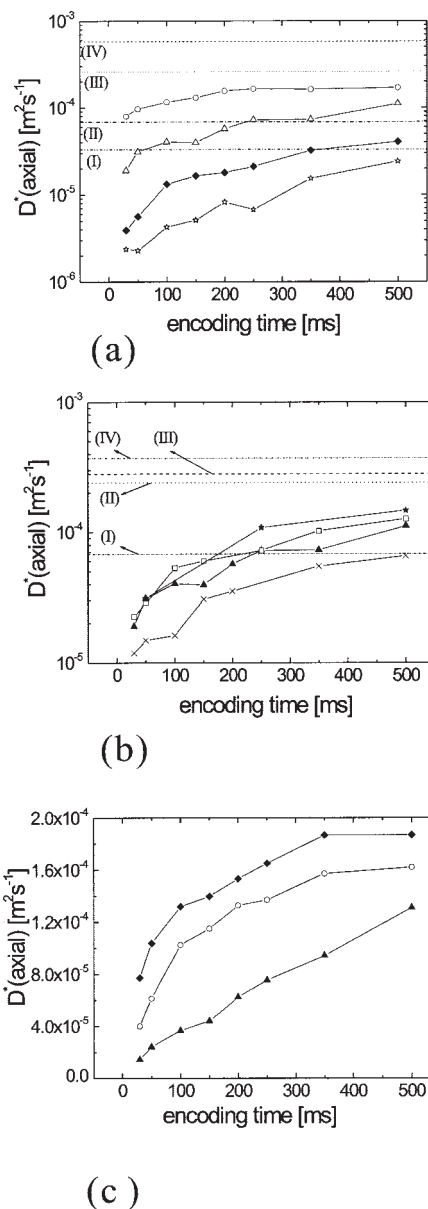

Figure 9. Time dependency of the axial dispersion coefficients D^* for water flow determined by NMR.

Horizontal lines indicate the asymptotic values obtained from classical tracer measurements. Lines connecting the symbols serve as guide to the eye only. Experimental uncertainties for the coefficients are estimated as ±15%. (a) Water flow in packs of 2-mm glass beads at different flow rates. ☆: $Q = 0.58$ cm³/s, Re = 7, line (I); ◆: $Q = 1.08$ cm³/s, Re = 13, line (II); △: $Q = 2.93$ cm³/s, Re = 36, line (III); ○: $Q = 6.33$ cm³/s, Re = 78, line (IV). (b) Water flow in packs of glass beads of different sizes, $Q = 2.93$ cm³/s (for $d_p = 0.6$ mm, $Q = 2.25$ cm³/s). ×: $d_p = 0.6$ mm, line (I); ▲: $d_p = 2$ mm, line (II); □: $d_p = 4$ mm, line (III); ★: $d_p = 7$ mm, line (IV). (c) Water flow in catalyst pellets (type C) at different flow rates. ▲: $Q = 2.93$ cm³/s; ○: $Q = 6.37$ cm³/s; ◆: $Q = 9.73$ cm³/s.

catalyst pellets of spherical or cylindrical shape of different sizes d_p. The packings were filled into tubes of circular cross section d_t, with the reduced dimensionless tube diameter d_t/d_p being varied in the range 1.4–32. The ordering of the pellet distribution, which is induced by the presence of the tube wall, was analyzed in terms of the fluid distribution in the saturated

fixed bed. Ordering effects were found even for nonspherical and polydisperse particles, and a maximum of the fluid density near the tube wall was confirmed for all pellet geometries and sizes.

The velocity distribution was found to behave in a way similar to that of the fluid density. Distinct maxima were observed in the radially averaged distributions, which coincided with the spin density maxima. For all but the smallest particles, where $d_t/d_p = 32$, the highest velocities occurred near the tube wall. The exact velocity distribution in an arbitrary slice across the model reactor, however, was found to be random, where the velocity distribution could best be described by a small number of individual backbone stems, with large fractions of the reactor volume not significantly taking part in the flow process. The efficiency of the reaction sites within the pellets is determined by this distribution of flow lines. The flow pattern, however, was demonstrated to change significantly as a function of volume flow rate even for a given bead array.

Statistical velocity distributions were obtained as a function of encoding time and averaged over a broad (25-mm) slice of the reactor. The contribution of the intraporous (static) fluid was found to be totally suppressed because of the relaxation properties inside the pellets. The decay of the stagnant, interparticle fluid fraction as a function of time is a feature critical to the efficiency of a fixed-bed reactor. As can be assumed from a diffusion-controlled process, the decay is faster for smaller pellet sizes, but possibly reduced further in a reactor of polydisperse cylindrical pellets. Fast flow near the tube wall does not contribute to the stagnant component but also reduces the conversion factor of the reactor because of its shorter contact with catalyst pellets.

The presented NMR techniques allowed us to follow the dispersion process in the preasymptotic region, that is, before the time-dependent longitudinal dispersion coefficient becomes constant. It is thus a suitable method to investigate the details of dispersion, reaction, and mixing processes on timescales < 1 s, which are not routinely accessible by conventional tracer techniques. Although averaged quantities such as the dispersion coefficient or the stagnant fluid fraction support a quantitative assessment of reactor efficiency, it is the spatially resolved methods, applied here for the first time to a wide range of aspect ratios an real catalyst pellets, that contribute detailed information about mass transport in the direct vicinity of the reaction sites.

Acknowledgments

Literature Cited

Ahn, B. J., A. Zoulalian, and J. M. Smith, "Axial Dispersion in Packed Beds with Large Wall Effect," *AIChE J.*, (1986)32, 170 .

Amin, M. H. G., S. J. Gibbs, R. J. Chorley, K. S. Richards, T. A. Carpenter, and L. D. Hall, "Study of Flow and Hydrodynamic Dispersion in a Porous Medium Using Pulsed-Field-Gradient Magnetic Resonance," *Proc. R. Soc. Lond. A*, **453**, 489 (1997).

Bey, O., and G. Eigenberger, "Fluid Flow through Catalyst Filled Tubes," *Chem. Eng. Sci.*, **52**, 1365 (1997).

Blümich, B., *NMR Imaging of Materials*, Oxford Univ. Press, Oxford, UK (2000).

Britton, M. M., R. G. Graham, K. J. Packer, "Relationships between Flow and NMR Relaxation of Fluids in Porous Solids," *Magn. Reson. Imaging*, **19**, 325 (2001).

Callaghan, P. T., *Principles of Nuclear Magnetic Resonance Microscopy*, Clarendon Press, Oxford, UK (1991).

Callaghan, P. T., and S. L. Codd, "Flow Coherence in a Bead Pack Observed Using Frequency Domain Modulated Gradient Nuclear Magnetic Resonance," *Phys. Fluids*, **13**, 421 (2001).

Callaghan, P. T., S. L. Codd, and J. D. Seymour, "Spatial Coherence Phenomena Arising from Translational Spin Motion in Gradient Spin Echo Experiments," *Concepts Magn Reson.*, **11**, 181 (2000).

Caprihan, A., and E. Fukushima, "Flow Measurements by NMR," *Phys. Rep.*, **198**, 195 (1990).

Carbonell, R. G., "Flow Non-Uniformities in Packed Beds: Effect on Dispersion," *Chem. Eng. Sci.*, **35**, 1347 (1980).

Chen, S. H., F. F. Qin, K. H. Kim, and A. T. Watson, "NMR Imaging of Multiphase Flow in Porous Media," *AIChE J.*, **39**, 925 (1993).

Codd, S. L., and S. A. Altobelli, "A PGSE Study of Propane Gas Flow through Model Porous Bead Packs," *J. Magn. Reson.*, **163**, 16 (2003).

Cotts, R. M., M. J. R. Hoch, T. Sun, and J. T. Marker, "Pulsed Field Gradient Stimulated Echo Methods for Improved NMR Diffusion Measurements in Heterogeneous Systems," *J. Magn. Reson.*, **83**, 252 (1989).

Damion, R. A., K. J. Packer, K. S. Sorbie, and S. R. McDougall, "Pore-Scale Network Modelling of Flow Propagators Derived from Pulsed Magnetic Field Gradient Spin Echo NMR Measurements in Porous Media," *Chem. Eng. Sci.*, **55**, 5981 (2000).

Feinauer, A., S. A. Altobelli, and E. Fukushima, "NMR Measurements of Flow Profiles in a Coarse Bed of Packed Spheres," *Magn. Reson. Imaging*, **15**, 479 (1997).

Fukushima, E., "Nuclear Magnetic Resonance as a Tool to Study Flow," *Annu. Rev. Fluid Mech.*, **31**, 95 (1999).

Gladden, L. F., "Applications of In Situ Magnetic Resonance Techniques in Chemical Reaction Engineering," *Topics Catal.*, **8**, 87 (1999).

Gladden, L. F., "Magnetic Resonance: Ongoing and Future Role in Chemical Engineering Research," *AIChE J.*, **49**, 2 (2003).

Gladden, L. F., M. H. M. Lim, M. D. Mantle, A. J. Sederman, and E. H. Stitt, "MRI Visualisation of Two-Phase Flow in Structured Supports and Trickle-Bed Reactors," *Catal. Today*, **79**, 203 (2003).

Gladden, L. F., M. D. Mantle, A. J. Sederman, and E. H. L. Yuen, "Magnetic Resonance Imaging of Single- and Two-Phase Flow in Fixed-Bed Reactors," *Appl. Magn. Reson.*, **22**, 201 (2002).

Götz, J., K. Zick, C. Heinen, and T. König, "Visualisation of Flow Processes in Packed Beds with NMR Imaging: Determination of the Local Porosity, Velocity Vector and Local Dispersion Coefficients," *Chem. Eng. Process.*, **41**, 611 (2002).

Hsiang, T. C., and H. W. Haynes, "Axial Dispersion in Small Diameter Beds of Large, Spherical Particles," *Chem. Eng. Sci.*, **32**, 678 (1977).

Kandhai, D., D. Hlushkou, A. G. Hoekstra, P. M. A. Sloot, H. Van As, and U. Tallarek, "Influence of Stagnant Zones on Transient and Asymptotic Dispersion in Macroscopically Homogeneous Porous Media," *Phys. Rev. Lett.*, **88**, 234501 (2002).

Khrapitchev, A. A., and P. T. Callaghan, "Reversible and Irreversible Dispersion in a Porous Medium," *Phys. Fluids*, **5**, 2649 (2003).

Khrapitchev, A. A., S. Stapf, and P. T. Callaghan, "NMR Visualisation of Displacement Correlations for Flow in Porous Media," *Phys. Rev. E*, **66**, 051203 (2002).

Klemm, A., R. Kimmich, and M. Weber, "Flow through Percolation Clusters: NMR Velocity Mapping and Numerical Simulation Study," *Phys. Rev. E*, **63**, 041514 (2001).

Klemm, A., H.-P. Müller, and R. Kimmich, "NMR Microscopy of Pore-Space Backbones in Rock, Sponge, and Sand in Comparison with Random Percolation Model Objects," *Phys. Rev. E*, **55**, 4413 (1997).

Koptyug, I. V., S. A. Altobelli, E. Fukushima, A. V. Matveev, and R. Z. Sagdeev, "Thermally Polarized ^{1}H NMR Microimaging Studies of Liquid and Gas Flow in Monolithic Catalysts," *J. Magn. Reson.*, **147**, 36 (2000).

Koptyug, I. V., L. Y. Ilyina, A. V. Matveev, R. Z. Sagdeev, V. N. Parmon, and S. A. Altobelli, "Liquid and Gas Flow and Related Phenomena in Monolithic Catalysts Studied by H-1 NMR Microimaging," *Catal. Today*, **69**, 385 (2001).

Kutsovsky, Y. E., L. E. Scriven, and H. T. Davis, "NMR Imaging of Velocity Profiles and Velocity Distributions in Bead Packs," *Phys. Fluids*, **8**, 863 (1996).

Lebon, L., J. Leblond, and J. P. Hulin, "Experimental Measurement of Dispersion Processes at Short Times Using a Pulsed Field Gradient NMR Technique," *Phys. Fluids*, **9**, 481 (1997).

Lebon, L., L. Oger, J. Leblond, J. P. Hulin, N. S. Martys, and L. M. Schwartz, "Pulsed Gradient NMR Measurements and Numerical Simulation of Flow Velocity Distribution in Sphere Packings," *Phys. Fluids*, **8**, 293 (1996).

Lucas, A. J., S. G. Gibbs, E. W. Jones, M. Peyron, A. D. Derbyshire, and L. D. Hall, "Diffusion Imaging in the Presence of Static Magnetic-Field Gradients," *J. Magn. Reson. A*, **104**, 273 (1993).

Maier, R. S., D. M. Kroll, R. S. Bernard, S. E. Howington, J. F. Peters, and H. T. Davis, "Pore-Scale Simulation of Dispersion," *Phys. Fluids*, **12**, 2065 (2000).

Maier, R. S., D. M. Kroll, R. S. Bernard, S. E. Howington, J. F. Peters, and H. T. Davis, "Enhanced Dispersion in Cylindrical Packed Beds," *Philos. Trans. R. Soc. Lond. A*, **360**, 497 (2002).

Maier, R. S., D. M. Kroll, H. T. Davis, and R. S. Bernard, "Simulation of Flow in Bidisperse Sphere Packings," *J. Colloid Interface Sci.*, **217**, 341 (1999).

Maier, R. S., D. M. Kroll, Y. E. Kutsovsky, H. T. Davis, and R. S. Bernard, "Simulation of Flow through Bead Packs Using the Lattice Boltzmann Method," *Phys. Fluids*, **10**, 60 (1998).

Mair, R. W., R. Wang, M. S. Rosen, D. Candela, D. G. Cory, and R. L. Walsworth, "Applications of Controlled-Flow Laser-Polarized Xenon Gas to Porous and Granular Media Study," *Magn. Reson. Imaging*, **21**, 287 (2003).

Mansfield, P., and M. Bencsik, "Stochastic Effects on Single Phase Fluid Flow in Porous Media," *Magn. Reson. Imaging*, **19**, 333 (2001).

Mansfield, P., and B. Issa, "Fluid Transport in Porous Rocks. I. EPI Studies and a Stochastic Model of Flow," *J. Magn. Reson. A*, **122**, 137 (1996).

Mantle, M. D., A. J. Sederman, and L. F. Gladden, "Single- and Two-Phase Flow in Fixed-Bed Reactors: MRI Flow Visualisation and Lattice-Boltzmann Simulations," *Chem. Eng. Sci.*, **56**, 523 (2001).

Manz, B., P. Alexander, and L. F. Gladden, "Correlations between Dispersion and Structure in Porous Media Probed by Nuclear Magnetic Resonance," *Phys. Fluids*, **11**, 259 (1999a).

Manz, B., L. F. Gladden, and P. B. Warren, "Flow and Dispersion in Porous Media: Lattice-Boltzmann and NMR Studies," *AIChE J.*, **45**, 1845 (1999b).

Martin, H., "Low Peclet Number Particle-to-Fluid Heat and Mass Transfer in Packed Beds," *Chem. Eng. Sci.*, **33**, 913 (1978).

Packer, K. J., and J. J. Tessier, "The Characterization of Fluid Transport in a Porous Solid by Pulsed Gradient Stimulated Echo NMR," *Mol. Phys.*, **87**, 267 (1996).

Papageorgiou, J. N., and G. F. Froment, "Simulation Models Accounting for Radial Voidage Profiles in Fixed-Bed Reactors," *Chem. Eng. Sci.*, **50**, 3043 (1995).

Park, J., and S. J. Gibbs, "Mapping Flow and Dispersion in a Packed Column by MRI," *AIChE J.*, **45**, 655 (1999).

Park, J. C., K. Raghavan, and S. J. Gibbs, "Axial Development and Radial Non-Uniformity of Flow in Packed Columns," *J. Chromatogr. A*, **945**, 65 (2002).

Seager, R. B., L. E. Scriven, and H. T. Davis, "Flow, Conduction, and a Characteristic Length in Periodic Bicontinuous Porous Media," *Phys. Rev. A*, **44**, 5087 (1991).

Sederman, A. J., P. Alexander, and L. F. Gladden, "Structure of Packed Beds Probed by Magnetic Resonance Imaging," *Powder Technol.*, **117**, 255 (2001).

Seymour, J. D., and P. T. Callaghan, " 'Flow-Diffraction' Structural Characterization and Measurement of Hydrodynamic Dispersion in Porous Media by PGSE NMR," *J. Magn. Reson.*, **122**, 90 (1996).

Seymour, J. D., and P. T. Callaghan, "Generalized Approach to NMR Analysis of Flow and Dispersion in Porous Media," *AIChE J.*, **43**, 2096 (1997).

Shattuck, M., R. Behringer, J. G. Georgiadis, and G. A. Johnson, "Magnetic Resonance Imaging of Interstitial Velocity Distributions in Porous Media," *Experimental Techniques in Multi-Phase Flows*, T. J. O'Hern, and R. A. Gore, eds., Vol. 121, p. 39, ASME, FED, New York (1991).

Shattuck, M., R. Behringer, G. A. Johnson, and J. G. Georgiadis, "Onset and Stability of Convection in Porous Media—Visualization by Magnetic Resonance Imaging," *Phys Rev Lett.*, **75**, 1934 (1995).

Sheppard, S., M. D. Mantle, A. J. Sederman, M. L. Johns, and L. F. Gladden, "Magnetic Resonance Imaging Study of Complex Fluid Flow in Porous Media: Flow Patterns and Quantitative Saturation Profiling of Amphiphilic Fracturing Fluid Displacement in Sandstone Cores," *Magn. Reson. Imaging*, **21**, 365 (2003).

Stapf, S., "NMR Investigations of Correlations between Longitudinal and Transverse Displacements in Flow through Random Structured Media," *Chem. Phys.*, **284**, 369 (2002).

Stapf, S., K. J. Packer, S. B'ekri, and P. M. Adler, "Two-Dimensional NMR Measurements and Numerical Simulations of Fluid Transport in Porous Rocks," *Phys. Fluids*, **12**, 566 (2000).

Stapf, S., K. J. Packer, R. G. Graham, J.-F. Thovert, and P. M. Adler, "Spatial Correlations and Dispersion for Fluid Transport through Packed Glass Beads," *Phys. Rev. E*, **58**, 6206 (1998).

Tallarek, U., E. Bayer, and G. Guiochon, "Study of Dispersion in Packed Chromatographic Columns by Pulsed Field Gradient Nuclear Magnetic Resonance," *J. Am. Chem. Soc.*, **120**, 1494 (1998b).

Tallarek, U., E. Bayer, D. van Dusschoten, T. Scheenen, H. Van As, G. Guiochon, and U. D. Neue, "Dynamic NMR Microscopy of Chromatographic Columns," *AIChE J.*, **44**, 1962 (1998c).

Tallarek, U., T. W. J. Scheenen, and H. Van As, "Macroscopic Heterogeneities in Electroosmotic and Pressure-Driven Flow through Fixed Beds at Low Column-to-Particle Diameter Ratio," *J. Phys. Chem. B*, **105**, 8591 (2001).

Tallarek, U., D. van Dusschoten, H. Van As, E. Bayer, and G. Guiochon, "Study of Transport Phenomena in Chromatographic Columns by Pulsed Field Gradient NMR," *J. Phys. Chem. B*, **102**, 3486 (1998a).

Tallarek, U., F. J. Vergeldt, and H. Van As, "Stagnant Mobile Phase Mass Transfer in Chromatographic Media: Intraparticle Diffusion and Exchange Kinetics," *J. Phys. Chem. B*, **103**, 7654 (1999).

Tessier, J. J., and K. J. Packer, "The Characterization of Multiphase Fluid Transport in a Porous Solid by Pulsed Gradient Stimulated Echo Nuclear Magnetic Resonance," *Phys. Fluids*, **10**, 75 (1998).

Tessier, J. J., K. J. Packer, J.-F. Thovert, and P. M. Adler, "NMR Measurements and Numerical Simulation of Fluid Transport in Porous Solids," *AIChE J.*, **43**, 1653 (1997).

Waggoner, R. A., and E. Fukushima, "Velocity Distribution of Slow Fluid Flows in Bentheimer Sandstone: An NMRI and Propagator Study," *Magn. Reson. Imaging*, **14**, 1085 (1996).